A VISIBLE AND INFRARED IMAGE FUSION METHOD BASED ON GHOST IMAGING

Ye Hualong

School of Electrical and Information Engineering
Changshu Institute of Technology
Suzhou 215500, China

Email: 2367272689 @ qq.com

Abstract

In the natural light imaging scene, it is often illuminated by a variety of wavelength light sources. To obtain images with better robustness and richer information, in this paper, we propose a method of visible and infrared image fusion based on ghost imaging, which fully combines the advantages of visible and infrared imaging. In fact, two single wavelength illumination information and detection values are used for correlation reconstruction, and then the target information is obtained, using the New Sum of Modified Laplacian. Due to the combination of the advantages of dual-wavelength imaging, as a result, complementary information on the same object can be collected to comprehensively reconstruct the information on the object and reproduce the complete detailed information, thus promoting the development of multi-wavelength fusion technology in the field of imaging.

Keywords: ghost imaging, visible imaging, infrared imaging, image fusion.

1. Introduction

Image fusion is an important part of image processing technology. It aims to process the image information obtained by different sensors at multiple levels and in various aspects to output of an image, that is more suitable for visible information reception or computer processing, analysis, and decision [1, 2]. Compared with the image of a single sensor, fusion image can obviously improve the lack of clarity and information and obtain the target and scene information more accurately, reliably, and comprehensively [3, 4]. As a new imaging method to acquire object imaging by using spatial intensity correlation, ghost imaging has advantages such as ultra-strong channel noise resistance, image optical reconstruction, and weak signal imaging [5–7]. With the rapid development of ghost imaging in recent years, a large number of studies on ghost imaging technology are conducted [8, 9], including computational ghost imaging [10], compressed sensing ghost imaging [11], blind ghost imaging [12], and quantum ghost imaging [13]. Currently, ghost imaging techniques are widely used because of their advantages, such as nonlocal, strong anti-interference ability, and high detection sensitivity [14–16].

Visible imaging and infrared imaging are two major branches in the current imaging field [17]. Infrared image has low resolution and poor resolution potential for human eyes. Due to the wavelength of light wave, long transmission distance, atmospheric attenuation, and other reasons, the infrared image has strong spatial correlation, low contrast, and blurred visible effect. Visible image sensor utilizes the varying ability of objects to reflect visible light for imaging. Visible image can fully reflect the details of the whole scene, with high contrast and resolution, and the image has good edge texture and other

---

details [18, 19]. However, visible imaging technology is easily affected by the environment, difficult to penetrate fog, rain, snow, dust, etc., and the detection distance is limited. Infrared imaging technology converts infrared band information beyond the observation of human eyes into visible information, which can well identify targets with long detection distance, but poor image contrast and insufficient detailed information [20, 21].

In this work, we propose a visible and infrared image fusion method based on ghost imaging (VIIF-GI), which fully combines the advantages of visible and infrared imaging. Two single wavelength illumination information and detection values are used for correlation reconstruction, and then the target information is obtained by using the New Sum of Modified Laplacian (NSML). Combined with the advantages of dual-wavelength imaging, the information content of the object can be reconstructed comprehensively, and the complete details can be reproduced.

2. Ghost Imaging

Ghost imaging is a new imaging model, which is different from traditional optical imaging. It can be measured in the reference optical path without objects and can reconstruct the spatial information distribution of objects placed in the signal optical path. A bucket detector at the end of the optical path detects the value of light intensity after diffraction through the object. The principle of ghost imaging is shown in Fig. 1.

The laser is irradiated vertically on the light modulator, such as SLM and DMD. The light modulator operates according to the input phase picture. Phase $\phi_i(x,y)$ follows the uniform distribution on $[0, 2\pi]$, and the light field distribution is

Fig. 1. The principle of ghost imaging.

$\{I_i(x,y)\}$. After modulation, the free diffraction of the spot is transmitted to the object $T(x,y)$ to be imaged. The diffraction as reflected light intensity values of the object are collected and calculated by the bucket detector to obtain a series of intensity distributions B_i. According to Fresnel propagation function, the calculation formulas read

$$B_i = \iint [I_i(x,y) \times T(x,y)]\, dx\, dy, \qquad I_i(x,y) = |E_{in}(x,y) \exp[j\varphi_i(x,y)] \otimes h(x,y,d)|,$$

$$E_{\mathrm{in}}(x,y) = \exp[j\varphi_i(x,y)] \otimes h(x,y,d), \qquad h(x,y,d) = \frac{\exp(j2\pi d/\lambda)}{jd\lambda} \exp\left[\frac{j\pi}{d\lambda}(x^2+y^2)\right],$$

$$(1)$$

where λ is the wavelength of the light source, $j = \sqrt{-1}$, $E_{\mathrm{in}}(x,y)$ represents the illumination intensity distribution after free space propagation for a distance of d, $h(x,y,d)$ is the impulse function described by Fresnel transformation, and $\otimes$ represents the convolution operation. Then the correlation function is used to reconstruct the original information of the object. The expression of this process is as follows:

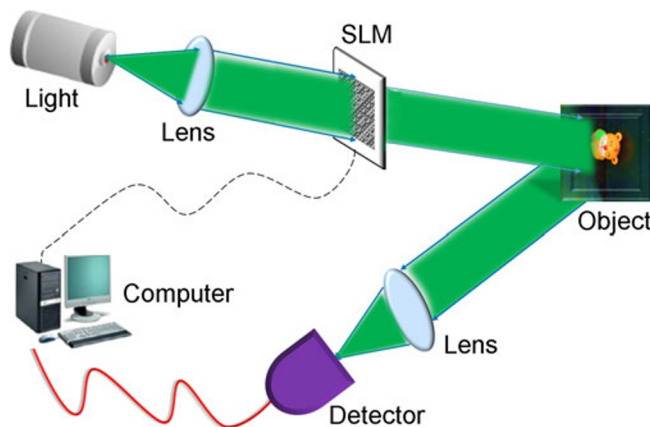$$T_{\mathrm{GI}}(x,y) = \frac{1}{N} \sum_{i=1}^{N} (B_i - \langle B \rangle)[I_i(x,y) - \langle I(x,y) \rangle], \qquad (2)$$

where $\langle B \rangle$ represents the average value of the bucket detector, N is the number of samples, and T_{GI} represents the image information of the reconstructed target.

3. Mechanism of Visible and Infrared Image Fusion Based on Ghost Imaging

The visible and infrared image fusion based on ghost imaging method, proposed in this paper, can fully combine the advantages of visible imaging and infrared imaging to reproduce more comprehensive image information. In Fig. 2, we presents the schematic diagram of the method proposed.
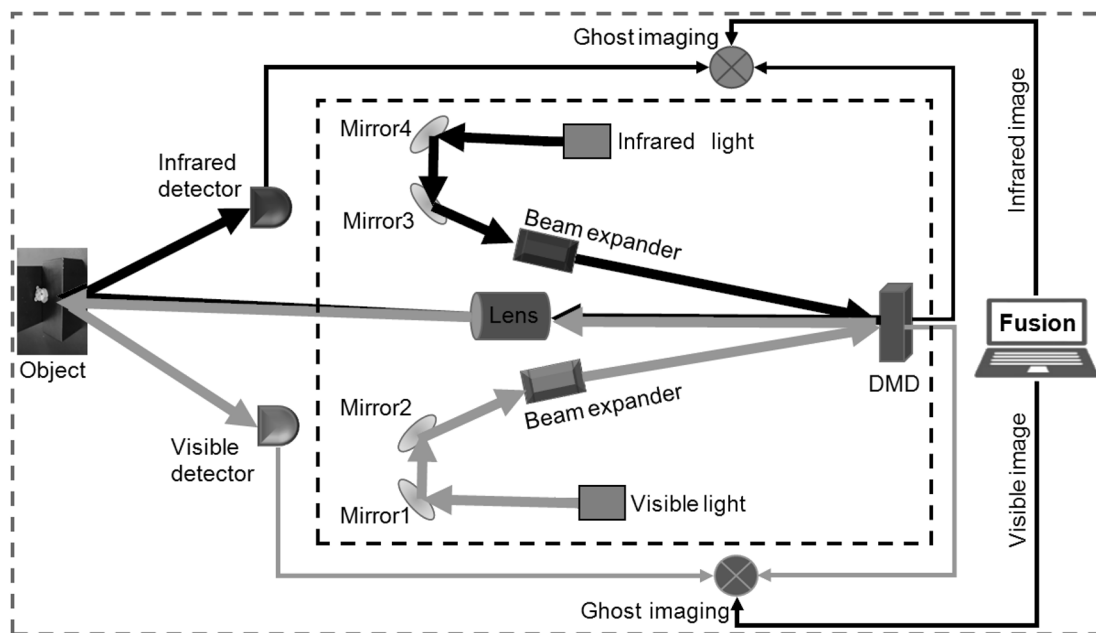

Fig. 2. Schematic diagram of visible and infrared image fusion method based on ghost imaging.

In this imaging algorithm, visible light and infrared light are used as illumination sources to irradiate the light modulator DMD, respectively. After DMD modulation, the light spot generated is transmitted to the object to be imitated $T(x, y)$, and the light intensity value received by the bucket detector is B_I,

$$
B_1 = \iint [I_1(x,y)T(x,y)]\, dx\, dy = \sum_{y=1}^{m} \sum_{x=1}^{n} I_1(x,y)T(x,y),
$$

$$
B_2 = \iint [I_2(x,y)T(x,y)]\, dx\, dy = \sum_{y=1}^{m} \sum_{x=1}^{n} I_2(x,y)T(x,y),
$$

(3)

where B_1 and B_2 represent the light intensity value received by infrared detector and visible detector, respectively, I_1 and I_2 represent the modulation matrix corresponding to band λ_1 and λ_2, respectively,

and m and n represent the size of the image, $N = m \times n$. Then Eq. (3) can also be expressed as follows:

$$B_1 = \sum_{y=1}^{m} \sum_{x=1}^{n} \left\{ \exp[j\varphi_i(x,y)] \otimes \frac{\exp(j2\pi d/\lambda_1)}{jd\lambda_1} \exp\left[\frac{j\pi}{d\lambda_1}(x^2 + y^2)\right] \right\}^2 T(x,y),$$

$$B_2 = \sum_{y=1}^{m} \sum_{x=1}^{n} \left\{ \exp[j\varphi_i(x,y)] \otimes \frac{\exp(j2\pi d/\lambda_2)}{jd\lambda_2} \exp\left[\frac{j\pi}{d\lambda_2}(x^2 + y^2)\right] \right\}^2 T(x,y).$$

(4)

Finally, the infrared information $T_1(x,y)$ and the visible information $T_2(x,y)$ of the object can be reconstructed by the correlation imaging function, i.e.,

$$T_1(x,y) = \frac{1}{N} \sum_{i=1}^{N} (B_{1i} - \langle B_1 \rangle) \left[I_{1i}(x,y) - \langle I_1(x,y) \rangle \right],$$

$$T_2(x,y) = \frac{1}{N} \sum_{i=1}^{N} (B_{2i} - \langle B_2 \rangle) \left[I_{2i}(x,y) - \langle I_2(x,y) \rangle \right].$$
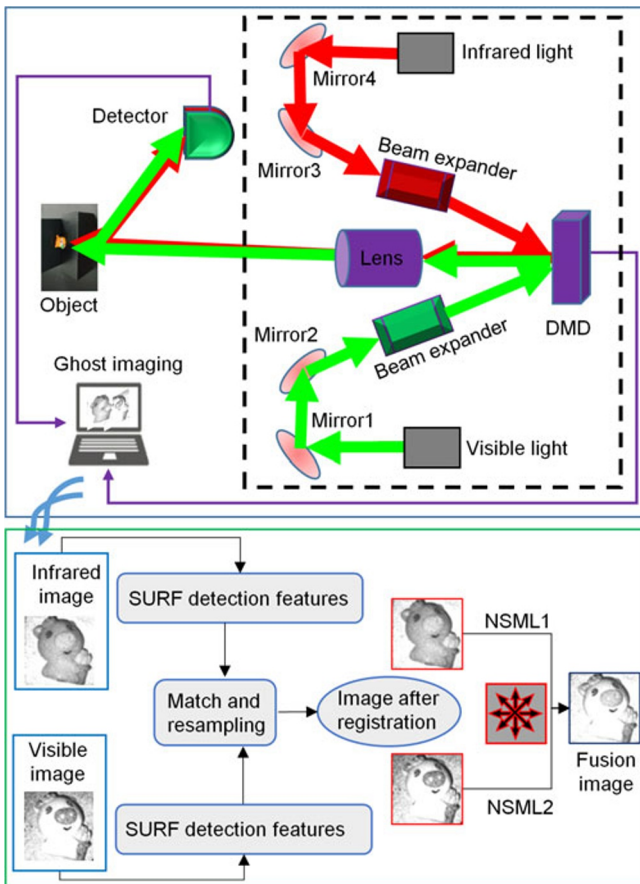
(5)

Fig. 3. Process diagram of visible and infrared image fusion method based on ghost imaging.

Then, the images are placed horizontally on the same axis, and the image registration method based on Speeded Up Robust Features (SURF) is adopted to achieve the matching calibration of infrared image and visible image. This method can effectively improve the accuracy of matching points and achieve high-precision registration of infrared image and visible image. SURF determines the matching degree by calculating the Euclidean distance between two feature points. The shorter the Euclidean distance, the better the matching degree of the two feature points. It consists of six steps: Feature detection; Determination of the main direction; Descriptor formation; Feature matching; Parameters estimation and re-sampling. The New Sum of Modified Laplacian (NSML) image fusion algorithm [22] is adopted to fuse the two and obtain the final reconstructed image; see Fig. 3.

In order to obtain better visible characteristics, more detailed information and prominent fusion effect, based on the traditional SML calculation of each pixel's variable step Laplace operator value of the only horizontal and vertical directions, four directions on the diagonal are added. The algorithm

is defined as follows:

$$
\begin{aligned}
\mathrm{ML}(x,y) &= |2I(x,y) - I(x-\text{step},y) - I(x+\text{step},y)| + |2I(x,y) - I(x,y-\text{step}) - I(x,y+\text{step})| \\
&\quad + |1.4I(x,y) - 0.7I(x-\text{step},y-\text{step}) - 0.7I(x+\text{step},y+\text{step})| \\
&\quad + |1.4I(x,y) - 0.7I(x+\text{step},y-\text{step}) - 0.7I(x-\text{step},y+\text{step})|, \\
\mathrm{NSML}(x,y) &= \sum\sum \mathrm{ML}(i,j).
\end{aligned}
\tag{6}
$$

In the eight directions of the NSML algorithm, the closer to the center pixel, the greater the contribution to ML, and the farther away from the center pixel, the smaller the contribution to ML. Therefore, the weight of contribution to ML from the horizontal and vertical directions is set as 1, and since the diagonal direction is farther from the center pixel than the horizontal and vertical directions, the corresponding weight of contribution to ML is set as 0.7. In formula (6), "step" is the variable step size parameter, and the cumulative window size of ML is $(2n+1)*(2n+1)$. Assume that $\mathrm{NSML}_1(x,y)$ and $\mathrm{NSML}_2(x,y)$ represents the definition of $T_1(x,y)$ and $T_2(x,y)$, respectively, then the fusion rules based on NSML algorithm are as follows:

$$
T'(x,y) = \begin{cases} T_1(x,y), & \mathrm{NSML}_1(x,y) > \mathrm{NSML}_2(x,y), \\ T_2(x,y), & \mathrm{NSML}_2(x,y) > \mathrm{NSML}_1(x,y). \end{cases}
\tag{7}
$$

4. Experimental Results and Analysis

In the experiment, the visible light source of 532 nm and the infrared light source of 1064 nm are used as the illumination field for imaging, and then the reconstructed images of the two are fused through the ghost imaging system, and finally the image close to the ideal is obtained. In the experimental results, the reconstruction targets "Pig" and "Cow" are taken as examples here. The imaging results under the visible reconstruction, infrared reconstruction, and fusion algorithm used in this paper are shown in Fig. 4.

In the quality evaluation of the image without reference, the clarity of the image is an important index to measure the quality of the image. It can better correspond to the subjective feeling of the person. The poor clarity of the image shows the blur of the image. In order to quantitatively analyze the image quality, two non-reference image quality evaluation functions, such as information entropy (EN) and spatial frequency (SF), are used to process and analyze the visible reconstructed image, infrared reconstructed image, and the fusion reconstruction effect, respectively.

4.1. Information Entropy

Information entropy (EN) is not equal to the amount of information, it is a measure of uncertainty caused by interference in the process of information transmission. It represents the discrete degree of pixel gray value in the fused image. Statistically speaking, the smaller the value is, the closer it is to uniform distribution, and the more balanced it is, the better the human vision is. We select the mean value of neighborhood gray level of the image as the spatial feature of gray level distribution, and the pixel gray level of the image forms a feature binary denoted as (i,j), where i represents the gray value of the pixel ($0 \le i \le 255$), and j represents the mean value of neighborhood gray level ($0 \le j \le 255$). Then
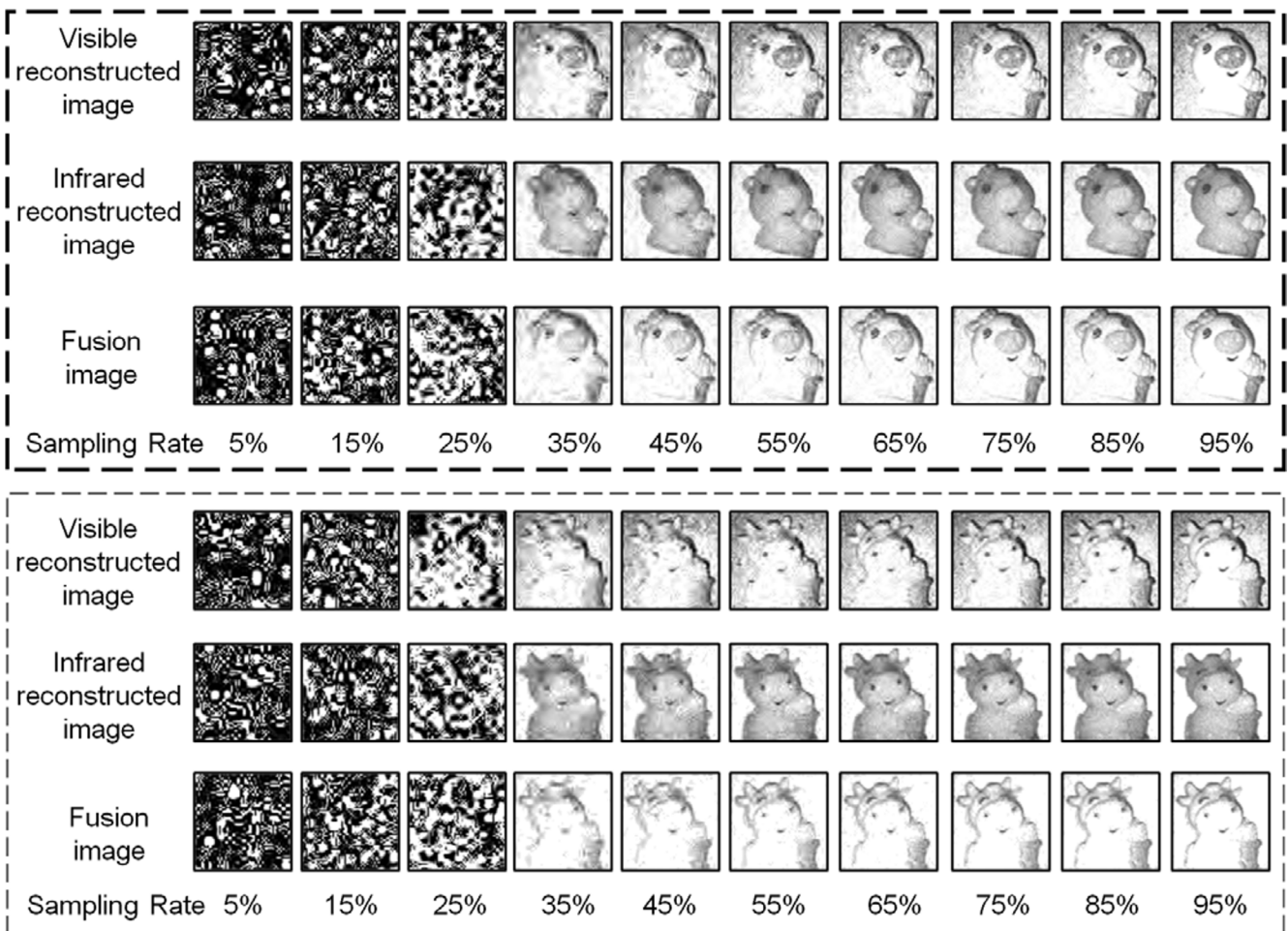
Fig. 4. Reconstruction effects at different sampling rates.

the calculation formula of information entropy reads

$$P_{i,j} = \frac{p(i,j)}{m \times n}, \qquad \mathrm{EN} = -\sum_{i}^{m} \sum_{j}^{n} P_{i,j} \lg P_{i,j}, \tag{8}$$

where $p(i,j)$ is the frequency of (i,j) and $m \times n$ is the scale size of the image. The EN changes of the reconstructed image of target "Pig" at different sampling rates (SR) are shown in Fig. 5 a, and the EN changes of the reconstructed image of target "Cow" at different SR are shown in Fig. 5 b.

As one can see in Fig. 5 a, with "Pig" as the target object, no matter which reconstruction method is adopted, EN value gradually decreases with the increasing sampling rate. For example, when SR is 15%, the EN value of image reconstructed by fusion algorithm is 3.611, and when SR is 95%, the EN value of image reconstructed by fusion algorithm is 2.4559. The higher the SR, the higher the accuracy of image reconstruction. As one can see in Fig. 5 b, "Cow" is used as the target object to reconstruct with different reconstruction algorithms. Although EN values of the three reconstruction algorithms all decreased with increase in SR, the EN values of the reconstruction effect of the proposed algorithm are lower than those of the visible reconstruction and infrared reconstruction, indicating that the reconstructed target image,
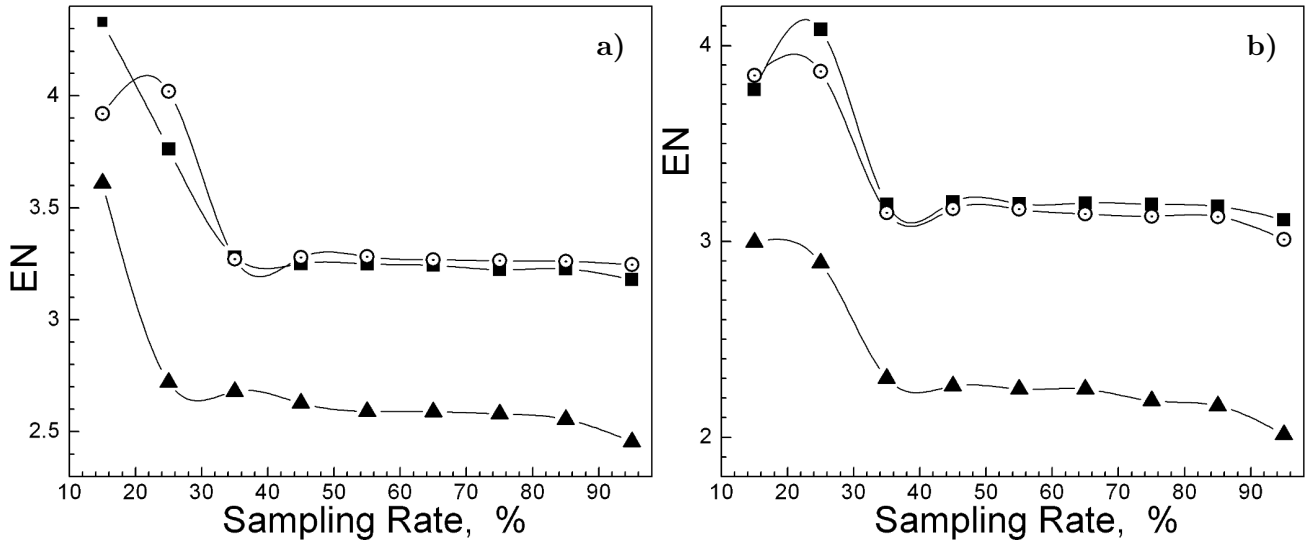
Fig. 5. EN of "Pig" (a) and "Cow" (b) reconstruction effect under algorithms: Visible-GI (■), Infrared-GI (⊙), and VIIF-GI (▲).

using the fusion algorithm in this paper, is in a more balanced state and has better visible effects.

4.2. Spatial Frequency

Spatial frequency (SF) is an image quality index based on horizontal gradient and vertical gradient. Horizontal gradient is also called spatial row frequency (RF), and vertical gradient is also called spatial column frequency (CF). Spatial frequency can effectively represent the gradient distribution of the image. The calculation formulas read

$$
\mathrm{RF} = \sqrt{\frac{1}{m \times n} \sum_{i=1}^{m} \sum_{j=2}^{n} (f_{i,j} - f_{i,j-1})^2}, \quad \mathrm{CF} = \sqrt{\frac{1}{m \times n} \sum_{i=2}^{m} \sum_{j=1}^{n} (f_{i,j} - f_{i-1,j})^2}, \quad \mathrm{SF} = \sqrt{\mathrm{RF}^2 + \mathrm{CF}^2},
$$
(9)

where $f_{i,j}$ is the gray value of the image pixel (i,j). The RF, CF, and SF values of visible reconstruction, infrared reconstruction, and fusion algorithm reconstruction are given in Table 1, and the changes between them are shown in Fig. 6.

One can see in Table 1 and Fig. 6 that the SF of the target image reconstructed by the VIIF-GI algorithm tends to be between the spatial frequencies of the Visible-GI and the Infrared-GI, and this is true for both the spatial RF and the CF. It shows that the fusion reconstruction effect of the algorithm in this paper is better than that of the visible reconstruction and infrared reconstruction, and the information is more complete.

5. Conclusions

In the natural light field imaging scene, there is often a variety of wavelengths of light field lighting. In order to better meet the requirements of human vision, in this paper, we proposed a visible and infrared image fusion method based on ghost imaging, which fully combines the advantages of visible imaging and

Table 1. Spatial Frequency of Reconstruction Effect under Different Algorithms.

		Visible-GI	Infrared-GI	VIIF-GI
Pig	RF	32.4965	28.5742	29.5435
	CF	25.0092	21.0676	22.9480
	SF	41.0059	35.5011	36.4423
Cow	RF	32.9436	22.6573	23.2186
	CF	32.1129	22.3675	22.8580
	SF	46.0056	32.1913	33.5821
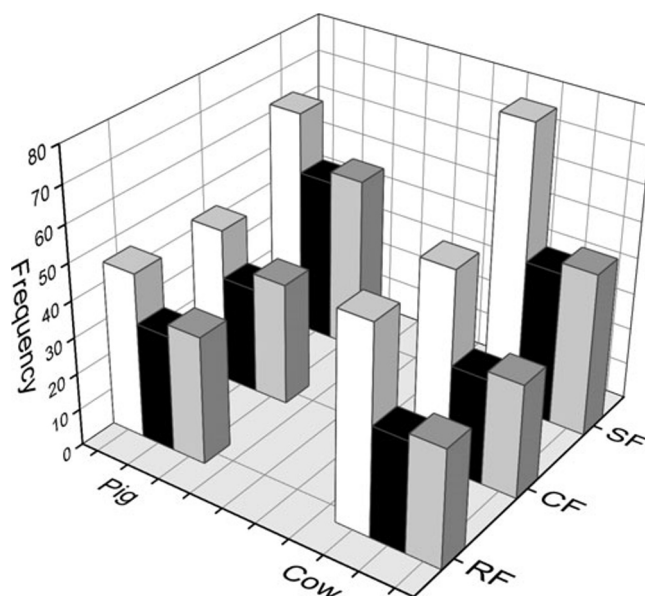
Fig. 6. Spatial frequency variation of the reconstruction effect under different algorithms: Visible-GI (white), Infrared-GI (black), and VIIF-GI (gray).

infrared imaging. Light sources at 532 and 1,064 nm were used as illumination sources for visible imaging and infrared imaging. We reconstructed two single wavelength illumination information and detection values by correlation, and then obtained the target information by fusion, using the NSML algorithm. Taking reconstruction targets "Pig" and "Cow" as examples, we analyzed the visible reconstructed image, infrared reconstructed image, and fusion reconstruction effect, in view of the corresponding analysis of two non-reference image quality evaluation functions, such as EN and SF. We obtained that, with the continuous increase in the sampling rate, the EN value gradually decreases and the accuracy of reconstructed image gradually increases. Moreover, the SF of the target image reconstructed by the algorithm in this paper tends to be between the SF of the visible reconstruction and the infrared reconstruction, indicating that the target image reconstructed by the fusion algorithm is in a more balanced state, with better visible effect and more complete information. This algorithm provides a theoretical basis for multi-wavelength fusion technology in imaging field and has a good application prospect.

Acknowledgments

References

1. Z. Qiang, L. Yi, S. Rick, et al., *Inf. Fusion*, **40**, 57 (2018); DOI: 10.1016/j.inffus.2017.05.006
2. Y. Zhang, M. Jin, and G. Huang, *Biomed. Signal Process. Control*, **74**, 103535 (2022).
3. J. Zuo, W. Zhao, L. Chen, et al., *Opt. Express*, **5**, 30 (2022).

4. Y. Hu, Z. Chen, B. Zhang, et al., *IET Image Process.*, **1**, 16 (2022).

5. P. A. Moreau, E. Toninelli, T. Gregory, et al., *Laser Photonics Rev.*, **1**, 12 (2018).

6. Y. Hualong and G. Daidou, *Opt. Lasers Eng.*, **171**, 107790 (2023).

7. W. Le and Z. Shengmei, *Photonics Res.*, **6**, 4 (2016).

8. Y. Ya, W. Chengyuan, L. Jun, et al., *Opt. Express*, **16**, 24 (2016).

9. Y. Hualong, Z. Leihong, and Z. Dawei, *Opt. Laser Technol.*, **137**, 106779 (2021).

10. W. Heng, W. Ruizhou, L. Changsheng, et al., *Opt. Commun.*, **454**, 124490 (2020).

11. Z. Xiang, C. Zhengdong, W. Yuan, et al., *Opt. Eng.*, **1**, 58 (2019).

12. A. M. Paniagua-Diaz, I. Starshynov, N. Fayard, et al., *Optica*, **4**, 6 (2019).

13. P. A. Moreau, E. Toninelli, P. A. Morris, et al., *Opt. Express*, **6**, 26 (2018).

14. S. Liansheng, C. Yin, T. Ailing, et al., *Opt. Lasers Eng.*, **8**, 107 (2018).

15. S. Dongfeng, Z. Jiamin, H. Jian, et al., *Opt. Lasers Eng.*, **102**, 100 (2018).

16. Y. Jian, C. Kehan, I. Abdullah, et al., *IEEE Access*, **8**, 23054 (2020).

17. C. A. Fuller, *Remote Sens.*, **19**, 14 (2022).

18. T. Sanocki, *J. Imaging*, **12**, 8 (2022).

19. W. Xiao, G. Sili, J. Lu, et al., *Acta Photonica Sinica*, **5**, 49 (2020).

20. L. Xiuli, M. A. Junhui, C. Dongqi, et al., *Infrared Technol.*, **9**, 41 (2019).

21. F. Hou, Y. Zhang, Y. Zhou, et al., *Sustainability*, **18**, 14 (2022).

22. S. Lim, M. Kim, J. Kang, et al., *IEEE Access*, **8**, 176330 (2020).